Title	Biocompatible Gold Nanoparticle Arrays Photodeposited on Periodically Proton Exchanged Lithium Niobate
Authors(s)	Carville, N. Craig, Neumayer, Sabine M., Manzo, Michele, Gallo, Katia, Rodriguez, Brian J.
Publication date	2016-07-07
Publication information	Carville, N. Craig, Sabine M. Neumayer, Michele Manzo, Katia Gallo, and Brian J. Rodriguez. “Biocompatible Gold Nanoparticle Arrays Photodeposited on Periodically Proton Exchanged Lithium Niobate.” ACS, July 7, 2016. https://doi.org/10.1021/acsbiomaterials.6b00264.
Publisher	ACS
Item record/more information	http://hdl.handle.net/10197/7797
Publisher's statement	This document is the Accepted Manuscript version of a Published Work that appeared in final form in ACS Biomaterials Science and Engineering, copyright © 2016 American Chemical Society after peer review and technical editing by the publisher. To access the final edited and published work see http://pubs.acs.org/doi/abs/10.1021/acsbiomaterials.6b00264.
Publisher's version (DOI)	10.1021/acsbiomaterials.6b00264

Biocompatible gold nanoparticle arrays photodeposited on periodically proton exchanged lithium niobate

N. Craig Carville,[a,b] *Sabine M. Neumayer,*[a,b] *Michele Manzo,*[c] *Katia Gallo,*[c] *and Brian J. Rodriguez*[a,b,*]

[a]School of Physics, University College Dublin, Belfield, Dublin 4, Ireland

[b]Conway Institute of Biomolecular and Biomedical Research, University College Dublin, Belfield, Dublin 4, Ireland

[c]Department of Applied Physics, KTH - Royal Institute of Technology, Roslagstullbacken 21, 106 91 Stockholm, Sweden

Keywords: ferroelectric, atomic force microscopy, photochemistry, metallic nanoparticles, metallic nanostructures, biocompatibility, patterning

Photodeposition of silver nanoparticles onto chemically patterned lithium niobate having alternating lithium niobate and proton exchanged regions has been previously investigated. Here, the spatially defined photodeposition of gold nanoparticles onto periodically proton exchanged lithium niobate is demonstrated. It is shown that the location where the gold nanoparticles form can be tailored by altering the concentration of $HAuCl_4$. This enables the possibility to sequentially deposit gold and silver in different locations to create bimetallic arrays. The cytocompatibility of photodeposited gold, silver, and bimetallic ferroelectric templates to osteoblast-like cells is also investigated. Gold samples provide significantly greater cell biocompatibility than silver samples. These results highlight a potential route for using photodeposited gold on lithium niobate as a template for applications in cellular biosensing.

Introduction

The polarization-dependent photochemistry of ferroelectric materials such as lithium niobate (LN), which can be tailored via domain engineering and chemical patterning, has been previously exploited to fabricate metallic nanoparticle arrays with potential applications in Raman-based sensing of molecules.[1–18] Chemical patterning by proton exchange of LN with a benzoic acid source through mask openings leads to the substitution of Li^+ ions in the LN with H^+ ions from the acid. This substitution modifies the optical and piezoelectric properties and reduces the polarization in the exposed regions.[19–22] In the case of a 1D mask, the proton exchange process results in a periodically proton exchanged LN (PPELN) surface with alternating stripes of PELN and LN. Due to the creation of the mask openings by reactive ion etching (RIE) and the lateral diffusion (LD) of protons under the mask, the PE area comprises RIE and LD regions.[12] Such PPELN templates have been widely used for the photodeposition of silver nanoparticles from $AgNO_3$ solution in the presence of super bandgap energy illumination (bandgap of LN ~ 3.9 eV[23]).[12,20,24,25] While the period, width, and height of the resulting structures can be tailored through the selection of doping, processing, and deposition conditions, the silver nanoparticles typically deposit preferentially in the LD region.[12,14,16,17] The reduction in polarization at the interface between LN and PE regions leads to an electric field tangential to the surface resulting in the accumulation of electrons in the LD region, which reduce the Ag^+ ions from solution.[12] Such silver nanoparticles have been shown to provide surface enhanced Raman scattering and luminescence of probe molecules.[13,15,26] While silver is known to provide enhanced surface plasmon coupling compared to, *e.g.*, gold and copper as a result of less damping of the plasmon resonance,[27] silver is cytotoxic to cells[28–31] and therefore has limited applications for cellular biosensing. Recently, LN has been shown to be cytocompatible with osteoblast cells[32] and in order to develop a PPELN template-based cellular biosensor, biocompatible metal nanoparticles are required. Here, the photodeposition of gold nanoparticles from aqueous $HAuCl_4$ onto PPELN templates is demonstrated and the cytocompatibility of osteoblasts with gold and silver nanoparticle arrays is compared. It is shown that the gold preferentially deposits in RIE regions depending on the Au^{3+} ion concentration, which allows bimetallic templates having alternating silver and gold nanoparticle arrays in the LD and RIE regions, respectively, to be fabricated. Furthermore, gold nanoparticles provide significantly greater cell biocompatibility than silver nanoparticles. These results allow the potential of photodeposited gold on PPELN templates to be explored for applications in cellular biosensing.

Materials and Methods

Materials

PPELN samples, having a period of 6.09 μm, were fabricated from 500 μm-thick z-cut congruent LN crystals (CasTech), as previously reported.[12,15,17,25,33] Exposure of the -z surface of the LN crystal to benzoic acid at 200°C for 24 hours through 2.0 μm wide RIE openings (Cl_2/Ar discharge) in a titanium mask led to the periodic proton exchange of Li^+ with H^+ ions. The LD under the mask resulted in a broadening of the PE width. The titanium mask was subsequently removed by etching in hydrofluoric acid for 10 seconds.

Photodeposition

Prior to photodeposition, the samples were sonicated for 20 minutes each in acetone, isopropanol, and deionized water before being dried with compressed nitrogen. 10^{-1}, 10^{-2}, 10^{-3}, 10^{-4}, and 10^{-5} M concentrations of aqueous $HAuCl_4$ (484385, Sigma Aldrich) were prepared. 10^{-3} M $NaHSO_3$ was used to alter the pH of the 10^{-1} M $HAuCl_4$ solution. The pH of each solution was measured using a calibrated pH meter (pH 210, Hannah Instruments). The PPELN sample was placed inside a Petri dish and 160 μl of $HAuCl_4$ was pipetted onto the surface. The sample was illuminated with a 254 nm UV light source (11SC-2, Spectroline) located 2 cm above the surface with a duration of 20 minutes. Silver nanoparticle arrays were fabricated using 10^{-2} M $AgNO_3$ and 20 minutes of UV exposure. Bimetallic samples were fabricated by first depositing gold (10^{-2} M $HAuCl_4$; 20 minutes exposure) in the RIE regions and then silver (10^{-2} M $AgNO_3$; 20 minutes exposure) in the LD regions. The PPELN templates were reused after cleaning the samples as described above with an additional step of gently rubbing the sample with isopropanol soaked lens paper in between the acetone and isopropanol sonication steps and verifying that the sample was clean using atomic force microscopy (AFM).

Surface Characterization

Amplitude modulation AFM (MFP-3D, Asylum Research) was used to probe the surface topography of each sample before and after photodeposition with cantilevers having a typical resonant frequency of ~ 310 kHz and spring constant of ~ 40 N/m (PPP-NCH, Nanosensors). Complementary surface morphology images were acquired using a scanning electron microscope (SEM) (S-4300, Hitachi) with a source voltage of 10 kV.

Cell Viability

For the cell biocompatibility study, all samples were sterilized prior to cell culture for 20 minutes each in acetone, isopropanol, milliQ water, and ethanol via sonication and exposed to ionized air (963E, 3M) for 10 seconds. An osteoblast cell line (MC3T3) was cultured in flasks (T75, Sigma-Aldrich) until ~ 90% confluence using alpha minimum essential medium (M8042, Sigma-Aldrich) and supplemented with 10% fetal bovine serum, 1% penicillin-streptomycin, 2% 2 mM L-glutamine, and 1% sodium pyruvate (Invitrogen) (i.e., the cell culture media). The samples were then placed in 12 well plates (Greiner bio-one) and immersed in 2 ml of media at 37°C prior to cell seeding (10,000 cells per well as determined using a hemocytometer (3100 Bright-Line, Hausser Scientific)). The samples were kept in an incubator (Thermo Scientific) at 37°C, with 95% humidity and 5% CO_2.

To observe the cell morphology, the actin cytoskeleton and nuclei of MC3T3 cells were fluorescently stained and imaged via fluorescence microscopy. Each sample was cultured for 1 and 4 days and the staining was carried out after incubation. The cell culture media was aspirated and the samples were rinsed with phosphate buffered saline (PBS) and fixed in 4% paraformaldehyde/PBS for 20 minutes at room temperature. The samples were then permeabilized with 0.1% Triton X-100/PBS for 5 minutes. The actin was stained with fluorescein isothiocyanate-labeled phalloidin (P5282, Sigma-Aldrich) at a 1:100 dilution in PBS for 20 minutes and the nuclei were stained with 4',6-diamidino-2-phenylindole (DAPI) (90229, Millipore) at a 1:1000 dilution in PBS for 5 minutes. After the permeabilization and staining steps, the samples were immersed in PBS for 5 minutes. Immersion was repeated two additional times in fresh PBS. The samples were imaged with a 10× objective (200M, Zeiss Axiovert). Image colorization was performed using ImageJ (NIH).

Results and Discussion

Photodeposition of Gold

The $HAuCl_4$ concentrations used and the measured pH values are shown in Table 1.

Table 1. $HAuCl_4$ Concentration and pH

$HAuCl_4$ concentration (M)	pH
10^{-5}	3.54
10^{-4}	2.82
10^{-3}	2.70
10^{-2}	2.40
10^{-1}	1.96

The AFM topography images of the PPELN surfaces before (Fig. 1(a)) and after (Fig. 1(b-f)) illumination for 20 minutes in different $HAuCl_4$ concentrations (10^{-5} – 10^{-1} M) were used to determine where gold deposited. The RIE, LD, and LN regions are indicated in Fig. 1(a). The darkest stripes correspond to the overetching of the surface by RIE and are adjacent to the raised LD regions associated with surface swelling during proton exchange.

For an $HAuCl_4$ concentration of 10^{-5} M (Fig. 1(b)), there appears to be trace amounts of deposition, most notably in the LD regions. For 10^{-4} M (Fig. 1(c)), gold deposition is noticeable in LN and LD regions. There may also be deposition in the RIE regions, however, the inhomogeneous RIE surface makes this difficult to determine absolutely. For 10^{-3} M (Fig. 1(d)) and 10^{-2} M (Fig. 1(e)) $HAuCl_4$, gold deposits preferentially in the RIE regions and appears enhanced at the edges of the RIE regions. SEM images (Fig. 2) of gold nanoparticle arrays on PPELN illustrate the relatively large area, reproducible nanoparticle patterning that can be achieved using 10^{-2} M $HAuCl_4$ and illumination for 20 minutes. For the highest concentration (10^{-1} M $HAuCl_4$), there does not appear to be any gold deposition.

These results can be partially understood from the valence of gold in $HAuCl_4$; unlike silver in $AgNO_3$, which requires one electron to reduce Ag^+, the reduction of Au^{3+} to Au^0 requires three electrons. For 10^{-4} M, the presence of gold nanoparticles suggests that photogenerated electrons are available at the surface to take part in the reduction reaction. With this result in mind, the absence of deposition for the low concentration (high pH (Table 1)) case implies there are too few Au^{3+} reaching the surface during illumination. The photogenerated electrons are likely screened by H^+ ions in the solution at $HAuCl_4$ concentrations of 10^{-3} and 10^{-2} M, as reported by Hanson for lithium tantalate,[34] explaining the absence of deposition in the LN and LD areas. The deposition in the RIE regions for 10^{-3} and 10^{-2} M requires some additional consideration.

To investigate the role of the RIE process on photodeposition, we also prepared samples using a chromium mask, in which periodic openings were etched using a mixture of Cl_2/O_2 instead of Cl_2/Ar. The chromium mask was subsequently removed using a chromium etchant. In PPELN samples prepared using Cl_2/O_2 discharges, gold did not deposit in the RIE region for the same concentration range studied. It is likely that Ar^+ ion bombardment leads to Ar^+ implantation and therefore that the presence of these defects influences the proton exchange process and/or photogeneration/photodeposition. Increased damage and modified electrical properties in RIE with Ar versus O_2 have been reported for other materials.[35]

For the highest concentration (lowest pH) solution studied (10^{-1} M), the photogenerated charge is screened by H^+ ions from the solution for LN, LD, and RIE areas. When the pH of the 10^{-1} M $HAuCl_4$ concentration solution was adjusted from 1.96 to 2.15 with the addition of 10^{-3} M $NaHSO_3$ via pipetting in 200 µl increments in order to reduce the H^+ concentration while keeping the Au^{3+} concentration the same, deposition occurred preferentially again in the RIE region (not shown; similar to Fig. 1(e), 10^{-2} M). This result highlights the important role of screening by H^+ in gold photodeposition experiments on ferroelectric surfaces.

Bimetallic Photodeposition

The tunability of the location of preferential gold deposition from LD to RIE regions provides an opportunity to deposit both gold and silver nanoparticle arrays on the same sample. Following gold deposition onto RIE regions using 10^{-2} M $HAuCl_4$ and illumination for 20 minutes, silver was deposited onto LD regions of the same sample using 10^{-2} M $AgNO_3$ for 20 minutes, resulting in a sample with adjacent gold and silver nanoparticle arrays (Fig. 3). An averaged line profile is shown in Fig. 3(b). Such bimetallic PPELN templates may have potential applications for sensing selective adsorption of different species or combining advantages of silver and gold, e.g., by exploiting the enhanced plasmon resonance of silver and the biocompatibility of gold.[36]

Cytocompatibility of Metallic Nanoparticle Arrays

To investigate the cytocompatibility of gold, silver, and bimetallic nanoparticle arrays on PPELN for, e.g., cellular biosensing applications, MC3T3 osteoblasts were cultured on each sample over 4 days and fluorescence microscopy was used to visualize the cells (Fig. 4). Cells adhered to and proliferated on PPELN in the absence of metal (Fig. 4(a-c)) and in the presence of gold nanoparticles (Fig. 4(d-f)). The cells on the PPELN surface without metal were nearly fully confluent by day 4 (Fig. 4(c)) whereas cells on the gold sample were fully confluent by day 4 (Fig. 4(f)), suggesting that osteoblasts are cytocompatible with both PPELN and gold nanoparticles on PPELN. The demonstrated cytocompatibility of PPELN may enable biophotonic applications that utilize the optical waveguide properties of PELN. However, in the presence of silver nanoparticle arrays (Fig. 4(g-i) without gold and Fig. 4(j-l) with gold), the cell number was reduced compared to the PPELN control, in agreement with reports on the cytotoxicity of silver.[29]

To quantify these fluorescence images, cell counting was performed via nuclei staining (Fig. 5). The gold nanoparticle array sample had significantly more cells than all samples after day 1 and day 4. By day 4, both the silver and the bimetallic nanoparticle array samples had significantly less cells compared to the gold nanoparticle array sample and PPELN control. The number of osteoblasts is slightly larger when gold and silver are present as opposed to silver alone. This suggests that it may be possible to tailor the cytocompatibility of the surface to an extent by changing the ratio of RIE to LD regions, and thereby the ratio of gold to silver, during the fabrication of the PPELN templates. These results are consistent with previous reports on enhanced osteoblast proliferation on gold surfaces,[37] however, the surface topography may also affect proliferation.[38] The topography of the gold nanoparticle arrays, presumably depending on their height, were found in some instances to provide anisotropic cues to the cells leading to preferential alignment parallel to the nanoparticle array (Fig. 6).

Conclusions

Whereas silver deposits preferentially on the LD regions of PPELN templates independent of the $AgNO_3$ concentration used, gold deposits preferentially in the RIE regions for 10^{-3} and 10^{-2} M $HAuCl_4$ concentrations. It was therefore possible to create bimetallic nanoparticle arrays having silver in the LD regions and gold in the RIE regions. Such metallic nanostructured templates may have applications for sensing metal-specific binding analytes or for tuning the plasmonic response of the substrate by controlling the ratio of gold to silver. The cytocompatibility of gold, silver, and bimetallic nanoparticle arrays on PPELN templates as well as of PPELN in the absence of metal was also investigated. Osteoblast cells did not proliferate on surfaces having silver nanoparticles; however, gold nanoparticle arrays were found to be cytocompatible and even to enhance cell proliferation compared to the PPELN without metal. Such gold nanoparticle array PPELN templates may have cellular biosensing applications.

AUTHOR INFORMATION

Corresponding Author

*Author to whom correspondence should be addressed. Electronic address:
brian.rodriguez@ucd.ie

Author Contributions

The manuscript was written through contributions of all authors. All authors have given approval to the final version of the manuscript.

ACKNOWLEDGMENT

This publication has emanated from research conducted with the financial support of the DGPP and NANOREMEDIES, which are funded under the Programme for Research in Third Level Institutions (PRTLI) Cycle 5 and cofunded by the European Regional Development Fund. This work was also supported by the Swedish Scientific Research Council (VR 622-2010-526 and 621-2011-4040) and the ADOPT Linnaeus Centre for Advanced Optics and Photonics in Stockholm. The AFM used for this work was funded by Science Foundation Ireland (SFI07/IN1/B931). An optical microscope in the UCD Conway Imaging Core Facility was used in this work.

REFERENCES

(1) Dunn, S.; Sharp, S.; Burgess, S. The photochemical growth of silver nanoparticles on semiconductor surfaces–initial nucleation stage. *Nanotechnology* **2009**, *20* (11), 115604 DOI: 10.1088/0957-4484/20/11/115604.

(2) Dunn, S.; Jones, P. M.; Gallardo, D. E. Photochemical growth of silver nanoparticles on c(–) and c(+) domains on lead zirconate titanate thin films. *J. Am. Chem. Soc.* **2007**, *129* (28), 8724–8728 DOI: 10.1021/ja071451n.

(3) Liu, X. Y.; Kitamura, K.; Terabe, K.; Hatano, H.; Ohashi, N. Photocatalytic nanoparticle deposition on $LiNbO_3$ nanodomain patterns via photovoltaic effect. *Appl. Phys. Lett.* **2007**, *91* (4), 044101 DOI: 10.1063/1.2759472.

(4) Liu, X. Y.; Ohuchi, F.; Kitamura, K. Patterning of surface electronic properties and selective silver deposition on $LiNbO_3$ template. *Funct. Mater. Lett.* **2008**, *1* (3), 177–182.

(5) Dunn, S.; Tiwari, D. Influence of ferroelectricity on the photoelectric effect of $LiNbO_3$. *Appl. Phys. Lett.* **2008**, *93* (9), 092905 DOI: 10.1063/1.2978195.

(6) Hanson, J. N.; Rodriguez, B. J.; Nemanich, R. J.; Gruverman, A. Fabrication of metallic nanowires on a ferroelectric template via photochemical reaction. *Nanotechnology* **2006**, *17* (19), 4946–4949 DOI: 10.1088/0957-4484/17/19/028.

(7) Tiwari, D.; Dunn, S. Photochemical reduction of Al^{3+} to Al^0 over a ferroelectric photocatalyst — $LiNbO_3$. *Mater. Lett.* **2012**, *79*, 18–20 DOI: 10.1016/j.matlet.2012.03.077.

(8) Liu, X.; Kitamura, K.; Yu, Q.; Xu, J.; Osada, M.; Takahiro, N.; Li, J.; Cao, G. Tunable and highly reproducible surface-enhanced Raman scattering substrates made from large-scale nanoparticle arrays based on periodically poled $LiNbO_3$ templates. *Sci. Technol. Adv. Mater.* **2013**, *14* (5), 055011 DOI: 10.1088/1468-6996/14/5/055011.

(9) Hnilova, M.; Liu, X.; Yuca, E.; Jia, C.; Wilson, B.; Karatas, A. Y.; Gresswell, C.; Ohuchi, F.; Kitamura, K.; Tamerler, C. Multifunctional protein-enabled patterning on arrayed ferroelectric materials. *ACS Appl. Mater. Interfaces* **2012**, *4* (4), 1865–1871 DOI: 10.1021/am300177t.

(10) Sun, Y.; Nemanich, R. J. Photoinduced Ag deposition on periodically poled lithium niobate: Wavelength and polarization screening dependence. *J. Appl. Phys.* **2011**, *109* (10), 104302 DOI: 10.1063/1.3580509.

(11) Sun, Y.; Eller, B. S.; Nemanich, R. J. Photo-induced Ag deposition on periodically poled lithium niobate: Concentration and intensity dependence. *J. Appl. Phys.* **2011**, *110* (8), 084303 DOI: 10.1063/1.3647752.

(12) Carville, N. C.; Manzo, M.; Damm, S.; Castiella, M.; Collins, L.; Denning, D.; Weber, S. A. L.; Gallo, K.; Rice, J. H.; Rodriguez, B. J. Photoreduction of SERS-active metallic nanostructures on chemically patterned ferroelectric crystals. *ACS Nano* **2012**, *6* (8), 7373–7380 DOI: 10.1021/nn3025145.

(13) Damm, S.; Carville, N. C.; Rodriguez, B. J.; Manzo, M.; Gallo, K.; Rice, J. H. Plasmon enhanced Raman from Ag nanopatterns made using periodically poled lithium niobate and periodically proton exchanged template methods. *J. Phys. Chem. C* **2012**, *116* (50), 26543–26550 DOI: 10.1021/jp310248w.

(14) Balobaid, L.; Craig Carville, N.; Manzo, M.; Collins, L.; Gallo, K.; Rodriguez, B. J. Photoreduction of metal nanostructures on periodically proton exchanged MgO-doped lithium niobate crystals. *Appl. Phys. Lett.* **2013**, *103*, 182904 DOI: 10.1063/1.4827541.

(15) Damm, S.; Craig Carville, N.; Manzo, M.; Gallo, K.; Lopez, S. G.; Keyes, T. E.; Forster, R. J.; Rodriguez, B. J.; Rice, J. H. Surface enhanced luminescence and Raman scattering from ferroelectrically defined Ag nanopatterned arrays. *Appl. Phys. Lett.* **2013**, *103* (08), 083105 DOI: 10.1063/1.4818910.

(16) Balobaid, L.; Carville, N. C.; Manzo, M.; Gallo, K.; Rodriguez, B. J. Direct shape control of photoreduced nanostructures on proton exchanged ferroelectric templates. *Appl. Phys. Lett.* **2013**, *102*, 042908 DOI: 10.1063/1.4789412.

(17) Carville, N. C.; Manzo, M.; Denning, D.; Gallo, K.; Rodriguez, B. J. Growth mechanism of photoreduced silver nanostructures on periodically proton exchanged lithium niobate: Time and concentration dependence. *J. Appl. Phys.* **2013**, *113* (18), 187212 DOI: 10.1063/1.4801963.

(18) Haussmann, A.; Milde, P.; Erler, C.; Eng, L. M. Ferroelectric lithography: bottom-up assembly and electrical performance of a single metallic nanowire. *Nano Lett.* **2009**, *9* (2), 763–768 DOI: 10.1021/nl8033784.

(19) Jackel, J. L.; Rice, C. E.; Veselka, J. J. Proton exchange for high-index waveguides in $LiNbO_3$. *Appl. Phys. Lett.* **1982**, *41* (7), 607.

(20) Manzo, M.; Laurell, F.; Pasiskevicius, V.; Gallo, K. Two-dimensional domain engineering in $LiNbO_3$ via a hybrid patterning technique. *Opt. Mat. Exp.* **2011**, *1* (3), 365–371.

(21) Manzo, M.; Denning, D.; Rodriguez, B.; Gallo, K. Piezoresponse force microscopy on proton exchanged $LiNbO_3$ layers. In *Lasers, Sources, and Related Photonic Devices*; OSA Technical Digest (CD); Optical Society of America: San Diego, CA, 2012; p IF1A.5.

(22) Neumayer, S. M.; Ivanov, I. N.; Manzo, M.; Kholkin, A. L.; Gallo, K.; Rodriguez, B. J. Interface and thickness dependent domain switching and stability in Mg doped lithium niobate. *J. Appl. Phys.* **2015**, *118* (22), 1–7 DOI: 10.1063/1.4936605.

(23) Prokhorov, A. M.; Kuzminov, I. U. S. *Physics and chemistry of crystalline lithium niobate*; Hilger: Bristol/New York, 1990.

(24) Roussev, R. V; Bhagavatula, V.; Himmelreich, J.; Becken, K.; Tingley, J. Reverse-proton-exchanged waveguide frequency doublers for green light generation. *Proc. SPIE*. 2011, p 79171Z – 79171Z – 15.

(25) Manzo, M.; Laurell, F.; Pasiskevicius, V.; Gallo, K. Electrostatic control of the domain switching dynamics in congruent $LiNbO_3$ via periodic proton-exchange. *Appl. Phys. Lett.* **2011**, *98* (12), 122910 DOI: 10.1063/1.3571559.

(26) Lal, S.; Link, S.; Halas, N. J. Nano-optics from sensing to waveguiding. *Nat. Photonics* **2007**, *1* (11), 641–648 DOI: 10.1038/nphoton.2007.223.

(27) Fernanda Cardinal, M.; Rodríguez-González, B.; Alvarez-Puebla, R. A.; Pérez-Juste, J.; Liz-Marzán, L. M. Modulation of localized surface plasmons and SERS response in gold dumbbells through silver coating. *J. Phys. Chem. C* **2010**, *114* (23), 10417–10423 DOI: 10.1021/jp102519n.

(28) Prabhu, S.; Poulose, E. K. Silver nanoparticles: mechanism of antimicrobial action, synthesis, medical applications, and toxicity effects. *Int. Nano Lett.* **2012**, *2* (1), 32 DOI: 10.1186/2228-5326-2-32.

(29) Albers, C. E.; Hofstetter, W.; Siebenrock, K. A.; Landmann, R.; Klenke, F. M. In vitro cytotoxicity of silver nanoparticles on osteoblasts and osteoclasts at antibacterial concentrations. *Nanotoxicology* **2013**, *7* (February), 30–36 DOI: 10.3109/17435390.2011.626538.

(30) Grosse, S.; Evje, L.; Syversen, T. Silver nanoparticle-induced cytotoxicity in rat brain endothelial cell culture. *Toxicol. In Vitro* **2013**, *27* (1), 305–313 DOI: 10.1016/j.tiv.2012.08.024.

(31) Asharani, P. V; Low Kah Mun, G.; Hande, M. P.; Valiyaveettil, S. Cytotoxicity and genotoxicity of silver nanoparticles in human cells. *ACS Nano* **2009**, *3* (2), 279–290.

(32) Carville, N. C.; Collins, L.; Manzo, M.; Gallo, K.; Lukasz, B. I.; McKayed, K. K.; Simpson, J. C.; Rodriguez, B. J. Biocompatibility of ferroelectric lithium niobate and the influence of polarization charge on osteoblast proliferation and function. *J. Biomed. Mater. Res. Part A* **2015**, *103*, 2540–2548 DOI: 10.1002/jbm.a.35390.

(33) Manzo, M.; Denning, D.; Rodriguez, B. J.; Gallo, K. Nanoscale characterization of β-phase $H_xLi_{1-x}NbO_3$ layers by piezoresponse force microscopy. *J. Appl. Phys.* **2014**, *116* (6), 066815 DOI: 10.1063/1.4891352.

(34) Hanson, J. N. Domain patterned ferroelectric surfaces for selective deposition via photochemical reaction, PhD Thesis, North Carolina State University, 2007.

(35) Pearton, S. J.; Chakrabarti, U. K.; Hobson, W. S. Reactive ion etching induced damage

in GaAs and AlGaAs using $C_2H_6/H_2/Ar$ or CCl_2F_2/O_2 gas mixtures. *J. Appl. Phys.* **1989**, *66* (5), 2061 DOI: 10.1063/1.344296.

(36) McKenzie, F.; Faulds, K.; Graham, D. Mixed metal nanoparticle assembly and the effect on surface-enhanced Raman scattering. *Nanoscale* **2010**, *2* (1), 78–80 DOI: 10.1039/B9NR00211A.

(37) Liu, D.; Zhang, J.; Yi, C.; Yang, M. The effects of gold nanoparticles on the proliferation, differentiation, and mineralization function of MC3T3-E1 cells in vitro. *Chin. Sci. Bull.* **2010**, *55* (11), 1013–1019 DOI: 10.1007/s11434-010-0046-1.

(38) Burke, G. A.; Rea, C. J.; Horgan, F. G.; Turkington, M.; Boyd, A. R.; Meenan, B. J. Osteoblast-like cell response to calcium phosphate coating chemistry and morphology on etched silicon surfaces. *J. Mater. Sci.: Mater. Med.* **2012**, *23* (3), 835–851 DOI: 10.1007/s10856-011-4542-x.

TOC Figure

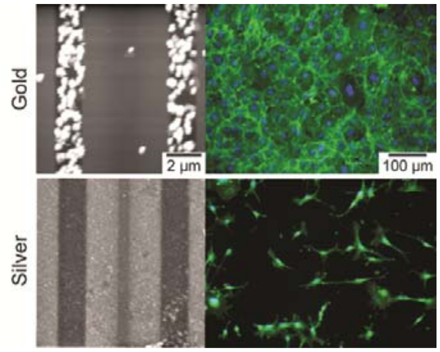

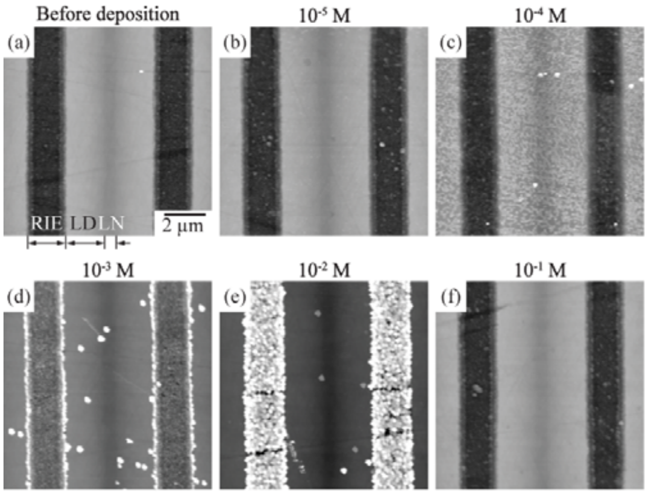

Fig. 1. (a) AFM topography image of a PPELN surface. (b-f) AFM topography images of PPELN surfaces after photodeposition using concentrations of 10^{-5} M, 10^{-4} M, 10^{-3} M, 10^{-2} M, and 10^{-1} M $HAuCl_4$, respectively. Data range for all AFM images is 50 nm.

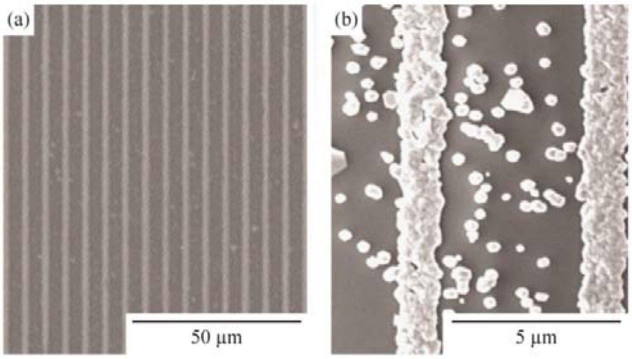

Fig. 2. (a, b) SEM images of gold nanoparticle arrays on PPELN templates.

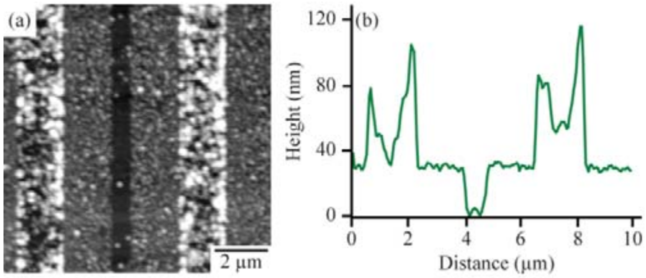

Fig. 3. (a) AFM topography image of a PPELN template with gold deposited on RIE regions and silver deposited on LD regions (120 nm data range). (b) Averaged line profile.

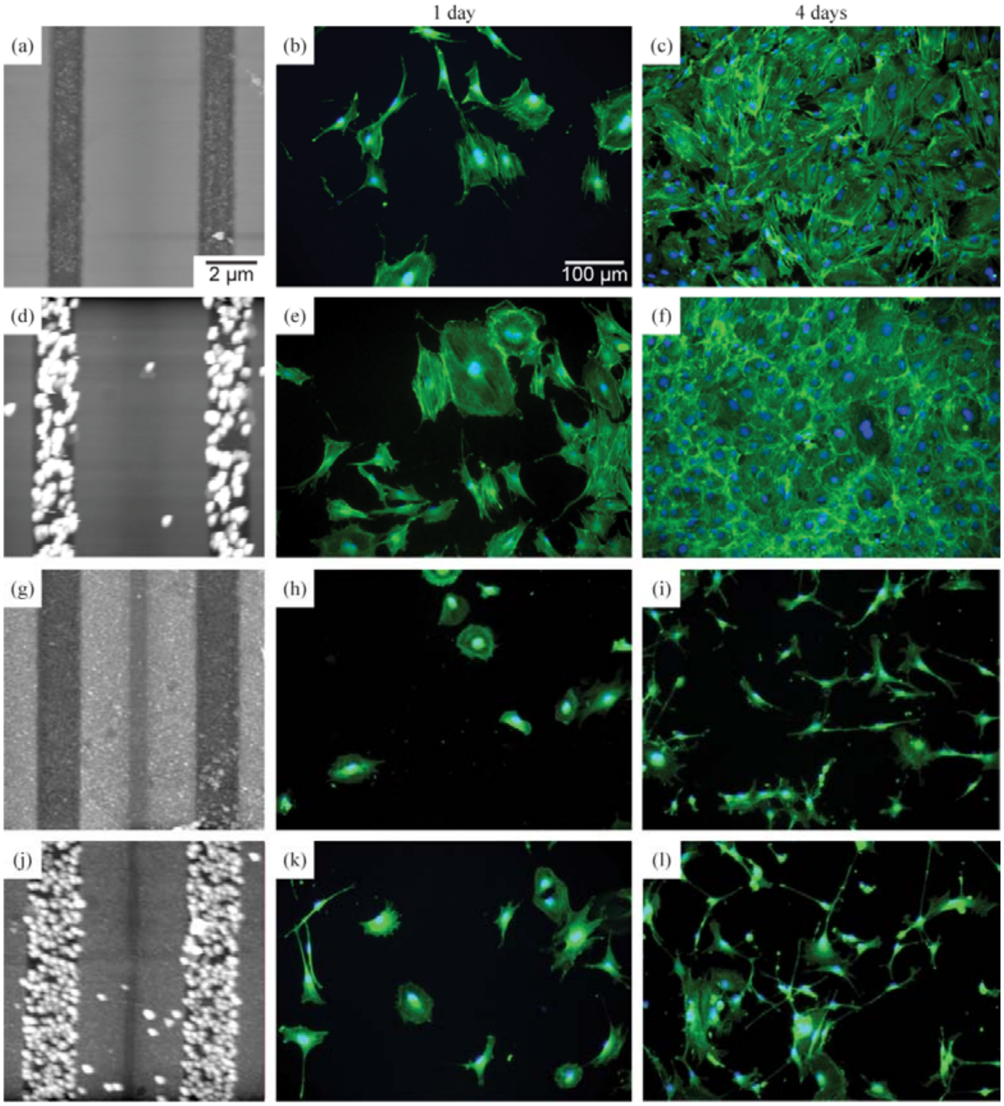

Fig. 4. AFM topography images of PPELN surfaces with (a) no deposition, (d) gold deposition, (g) silver deposition, and (j) gold and silver bimetallic deposition (150 nm data range). Representative fluorescent images of MC3T3 osteoblast cells (nuclei (DAPI, blue) and actin (phalloidin, green)) on each sample for day 1 and day 4 for (b, c) no deposition, (e, f) gold deposition, (h, i) silver deposition, and (k, l) gold and silver bimetallic deposition. The direction of the nanoparticle arrays in the fluorescent images matches that of the AFM images.

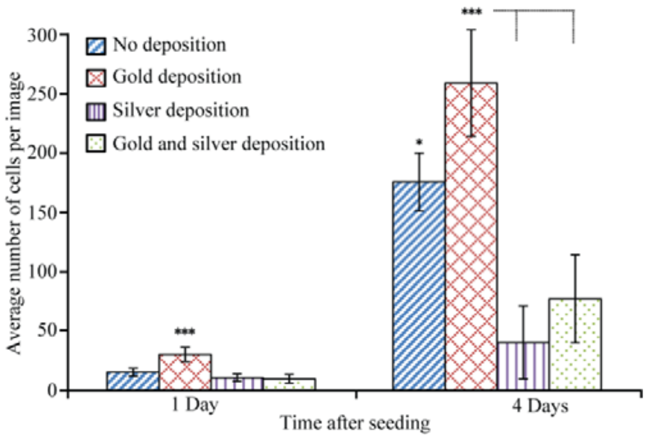

Fig. 5. Average number of cells obtained from fluorescence images using ImageJ cell-count macro illustrating MC3T3 osteoblast cell proliferation at day 1 and day 4 (* = p <0.01, *** = p<0.001).

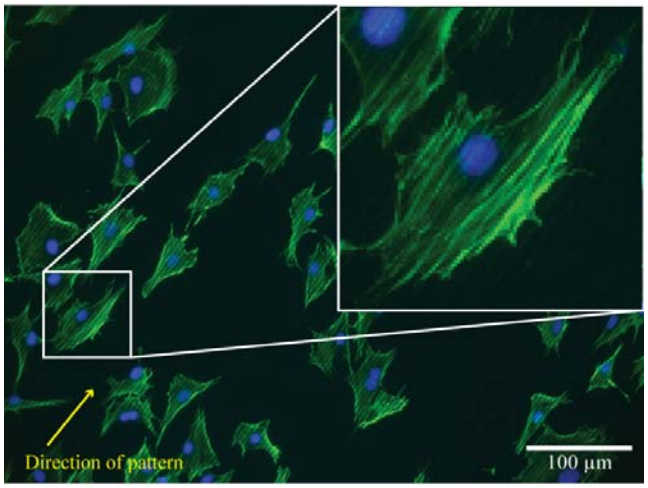

Fig. 6. Fluorescent image of MC3T3 osteoblast cells (nuclei (DAPI-blue) and actin (phalloidin-green)) on PPELN surfaces with gold deposition showing the alignment of actin parallel to the gold nanoparticle array (direction indicated with yellow arrow).